

A Novel Preunmixing Framework for Efficient Detection of Linear Mixtures in Hyperspectral Images

Andrea Marinoni, *Senior Member, IEEE*, Antonio Plaza, *Fellow, IEEE*, and Paolo Gamba, *Fellow, IEEE*

Abstract—In order to provide reliable information about the instantaneous field of view considered in hyperspectral images through spectral unmixing, understanding the kind of mixture that occurs over each pixel plays a crucial role. In this paper, in order to detect nonlinear mixtures, a method for fast identification of linear mixtures is introduced. The proposed method does not need statistical information and performs an *a priori* test on the spectral linearity of each pixel. It uses standard least squares optimization to achieve estimates of the likelihood of occurrence of linear combinations of endmembers by taking advantage of the geometrical properties of hyperspectral signatures. Experimental results on both real and synthetic data sets show that the aforesaid algorithm is actually able to deliver a reliable and thorough assessment of the kind of mixtures present in the pixels of the scene.

Index Terms—Nonorthogonal projection, remote sensing, spectral analysis, spectral unmixing.

I. INTRODUCTION

SPECTRAL unmixing (UMX) involves the estimation of pure spectral signatures (endmembers) and their corresponding abundances on each pixel for a hyperspectral scene. Nonlinear UMX has become of great importance due to the complexity of the mixtures appearing in the scenes [1]–[8]. As hyperspectral scenes may consist of heterogeneous reflectance schemes, UMX algorithms should be designed to be flexible and adaptive to properly fit and track the several interactions among materials [9]. Thus, the need of *a priori* tests for nonlinearity detection has become urgent. Therefore, reliable detection of nonlinear reflectance behavior can play a key role in enhancing hyperspectral UMX performance [1]–[5].

Recently, several papers have addressed the issue of nonlinearity detection under different assumptions on the models, environments, and structures. Typically, they rely on statistical properties of the hyperspectral image [10], Markov random

fields operating on spatial features [11], or Monte Carlo algorithms applied to the whole data set [12]. Instead, in [9] a framework for efficient p -linear UMX that considers a preprocessing step to estimate the nonlinearity order of each pixel by artificial neural network was introduced.

Although the aforementioned methods might actually provide enhancement in understanding and quantifying the nonlinear reflectance interactions, computational complexity still represents an issue for their actual implementation and development [4], [5], [9], [13]. Indeed, they basically look for an inversion of either linear or nonlinear mixture models in order to obtain the error distribution. Then, the nonlinear effect detection strongly relies on statistical, stochastic, and Bayesian functions of this distribution. Therefore, all estimates proposed in [10]–[12] and [14] represent *a posteriori* tests.

These frameworks are computationally expensive, as they require to run at least two UMX algorithms to detect nonlinearities. Furthermore, they rely on several approximations in terms of modeling, statistics, and nonlinear interactions. Hence, there is a need for novel methods able to perform computationally lighter *a priori* investigations able to deliver reliable estimates of nonlinear effects.

In this paper, instead of looking for nonlinearly mixed pixels, we develop a detector of linear mixtures. Specifically, taking advantage of the least squares optimization carried over linear and second-order combinations of endmembers, the proposed algorithm aims at delivering likelihood estimates of the occurrence of a linear mixing in each pixel. We also provide a new metric for estimating the actual ability of the chosen set of endmembers to thoroughly describe the interactions occurring over the considered scene. By taking advantage of the properties of nonorthogonal projections and the relationships among volumes of subspaces spanned by a set of spectra, it is possible to derive a measure of the efficiency of the system to characterize the combinations of materials. The experimental results on synthetic and real data sets show that the aforesaid algorithm works efficiently and without a major computational effort.

This paper is organized as follows: Section II reports the description of the proposed method, while Section III analyzes the experimental results. Finally, Section IV provides some final remarks.

II. METHODS

Let $\underline{Y} = \{\underline{y}_l\}_{l=1,\dots,P}$ be a P -pixel image, where $\underline{y}_l = [y_{ln}]_{n=1,\dots,N}$ is the N -band spectral signature of the l th pixel. Then, let $\mathcal{M} = \{\underline{m}_r\}_{r=1,\dots,R}$ be the set of the endmembers that

Manuscript received June 21, 2016; revised November 18, 2016 and February 1, 2017; accepted March 24, 2017. Date of publication April 27, 2017; date of current version July 20, 2017. The work of A. Marinoni, A. Plaza, and P. Gamba, “On the detection of linear mixtures in hyperspectral images,” was presented at the IEEE IGARSS 2016, Beijing, China. (Corresponding author: Andrea Marinoni.)

A. Marinoni and P. Gamba are with the Telecommunications and Remote Sensing Laboratory, Department of Electrical, Computer and Biomedical Engineering, University of Pavia, 27100 Pavia, Italy (e-mail: andrea.marinoni@unipv.it; paolo.gambag@unipv.it).

A. Plaza is with the Hyperspectral Computing Laboratory, Department of Computer Technology and Communications, University of Extremadura, 10003 Cáceres, Spain (e-mail: aplaza@unex.es).

Color versions of one or more of the figures in this paper are available online at <http://ieeexplore.ieee.org>.

Digital Object Identifier 10.1109/TGRS.2017.2691319

can be drawn over \underline{Y} according to an endmember extraction algorithm (EEA). Moreover, let us consider the fully constrained least squares (FCLS) [15] optimization algorithm in order to unmix the given image. Hence, when we run FCLS over the l th pixel considering the endmembers spectra in \mathcal{M}

$$\underline{y}_l = \hat{\underline{y}}_l^{(L)} + \hat{\underline{n}}_l = \sum_{r=1}^R \hat{a}_{lr} \underline{m}_r + \hat{\underline{n}}_l \quad (1)$$

where $\hat{a}_{lr} = [\hat{a}_{lr}]_{r=1, \dots, R}$ are the linear mix coefficients estimated by the FCLS, $\sum_{r=1}^R \hat{a}_{lr} = 1$ and $\hat{a}_{lr} \geq 0 \forall r$. Moreover, $\hat{\underline{n}}_l$ is the noise residual that results from the FCLS linear UMIX. Note that $\hat{\underline{y}}_l^{(L)}$ is the best linear approximation of \underline{y}_l by employing FCLS UMIX.

Let us consider now the set \mathcal{M}' of the spectral signatures provided by the extracted endmembers and their second-order combinations, i.e., $\mathcal{M}' = \mathcal{M} \cup \mathcal{M}^{(2)}$, where $\mathcal{M}^{(2)} = \{\mathcal{M}_{r'}^{(2)}\}_{r'=1, \dots, (R(R-1)/2)}$ represents the set of all possible second-order combinations ($\underline{m}_u \odot \underline{m}_v$) of endmember signatures in \mathcal{M} . Running again FCLS, the decomposition becomes

$$\underline{y}_l = \hat{\underline{y}}_l^{(L)} + \hat{\underline{y}}_l^{(NL)} + \hat{\underline{n}}_l = \sum_{r=1}^R \hat{a}'_{lr} \underline{m}_r + \sum_{r'=1}^{\frac{R(R-1)}{2}} \hat{\beta}'_{lr'} \mathcal{M}_{r'}^{(2)} + \hat{\underline{n}}_l \quad (2)$$

where $\hat{a}'_{lr} = [\hat{a}'_{lr}]_{r=1, \dots, R}$ and $\hat{\beta}'_{lr'} = [\hat{\beta}'_{lr'}]_{r'=1, \dots, (R(R-1)/2)}$ are the coefficients that drive the linear and bilinear mix as estimated by the FCLS, respectively, and $\sum_{r=1}^R \hat{a}'_{lr} + \sum_{r'=1}^{(R(R-1)/2)} \hat{\beta}'_{lr'} = 1$, $\hat{a}'_{lr} \geq 0 \forall r$, $\hat{\beta}'_{lr'} \geq 0 \forall r'$. Note that $\hat{\underline{n}}_l$ is the noise residual that results when FCLS UMIX based on second-order combinations of endmember spectra is used.

Let us now assume that the l th pixel indeed results from a linear combination of the endmembers' spectra in \mathcal{M} , i.e., $\underline{y}_l = \sum_{r=1}^R a_{lr} \underline{m}_r + \underline{n}_l$. In that case, the following equation holds: $\lim_{\|\underline{n}_l\|^2 \downarrow 0} \|\hat{\underline{y}}_l^{(L)} - \hat{\underline{y}}_l^{(NL)}\|^2 \approx 0$. In other words, when the l th pixel represents a linear mixture of the R endmembers in the scene, the contribution provided by $\hat{\underline{y}}_l^{(NL)}$ in (2) should be negligible. Therefore, in order to understand whether the l th pixel can be considered as a result of linear combinations of reflectances, in the ideal case (i.e., when the pixel noise is not relevant), one can just compute the Euclidean distance between $\hat{\underline{y}}_l^{(L)}$ and $\hat{\underline{y}}_l^{(NL)}$ and call for a linear mixture on the l th pixel if it is equal to zero.

On the other hand, if the noise spectrum is such that $\|\underline{n}_l\|^2 \downarrow n^* > 0$, then the aforementioned property does not hold anymore. Instead, $\lim_{\|\underline{n}_l\|^2 \downarrow n^*} \|\hat{\underline{y}}_l^{(L)} - \hat{\underline{y}}_l^{(NL)}\|^2 = \delta^* \geq 0$. It is worth to note that the final aim of statistical approaches such as those delivered in [10]–[12] is to properly detect the value of $\delta^* \forall l$ such that the kind of the mixtures in the given image is accurately evaluated. Thus, in order to estimate the correct threshold value of δ^* that we could use in order to discriminate between the occurrence of linear or nonlinear combination of endmembers in the l th pixel, we need a different approach. In order to retrieve a reliable and efficient metric such that no *a posteriori* estimate of the kind of mixture the l th pixel

displays is drawn out, we may consider the difference between $\hat{\underline{y}}_l^{(L)}$ and $\hat{\underline{y}}_l^{(NL)}$ from a geometrical point of view. Let us define $\hat{\underline{y}}_l^{(L)} - \hat{\underline{y}}_l^{(NL)} = \hat{\underline{D}}_l = \sum_{r=1}^R \hat{\delta}_{lr} \underline{m}_r$, where $\hat{\delta}_{lr} = \hat{a}_{lr} - \hat{a}'_{lr}$ and $\hat{\delta}_l = [\hat{\delta}_{lr}]_{r=1, \dots, R}$, with $\|\hat{\underline{D}}_l\|^2 = \delta^*$. Considering (1) and (2), the following equation holds:

$$\hat{\underline{D}}_l = \hat{\underline{y}}_l^{(NL)} + \hat{\underline{d}}_l^{(n)} = \hat{\underline{y}}_l^{(NL)} + (\hat{\underline{n}}_l - \hat{\underline{n}}_l). \quad (3)$$

Therefore, if most of the $\hat{\underline{D}}_l$ displacement is collected by the nonlinear contributions in $\hat{\underline{y}}_l^{(NL)}$, then the l th pixel represents a nonlinear combination of the endmembers in the scene. On the other hand, if the $\hat{\underline{D}}_l$ difference is mostly delivered by the noise residual difference in $\hat{\underline{n}}_l - \hat{\underline{n}}_l$, then we can assume that the nonlinear contributions as estimated by FCLS is negligible and the mixture is linear.

Now, since each $\hat{\underline{D}}_l$ is defined as a weighted sum of the endmembers in \mathcal{M} , we can consider $\hat{\delta}_{lr}$ as the projection of the displacement $\hat{a}_{lr} - \hat{a}'_{lr}$ onto the basis of the \mathcal{M} -induced subspace in the direction of the r th endmember. In order to obtain a coherent computation for volume comparison onto a consistent domain, it is thus necessary to evaluate the contribution provided by $\hat{\underline{y}}_l^{(NL)}$ and $\hat{\underline{d}}_l^{(n)}$ onto each endmember basis of the \mathcal{M} vectorial field [16], by rewriting (3) as follows:

$$\hat{\underline{D}}_l = \sum_{r=1}^R \hat{\delta}_{lr} \underline{m}_r = \sum_{r=1}^R \pi_r(\hat{\underline{y}}_l^{(NL)}) \underline{m}_r + \sum_{r=1}^R \pi_r(\hat{\underline{d}}_l^{(n)}) \underline{m}_r \quad (4)$$

where $\pi_r(\underline{z})$ identifies the nonorthogonal projection of \underline{z} onto the direction imposed by the r th endmember. Indeed, since typically the endmembers in \mathcal{M} are far from being perfectly orthogonal to each other, the computation of the π_r coefficients in (4) cannot be performed according to orthogonal projection algorithms, but a proper system of linear equations can be set up by taking advantage of the properties of Clifford algebra [16]. Specifically, let us consider an N -element array $\underline{z} = \sum_{r=1}^R \pi_r(\underline{z}) \underline{m}_r$. Then, let us consider R linear equations obtained by considering the inner product of \underline{z} onto an endmember ($\underline{z} \cdot \underline{m}_i = \sum_{r=1}^R \pi_r(\underline{z}) \underline{m}_r \cdot \underline{m}_i \forall i = 1, \dots, R$). The whole system in matrix form is $\underline{A}_{\mathcal{M}} \times \underline{\pi}(\underline{z})^T = \underline{b}^T$, where $\underline{A}_{\mathcal{M}} = \{A_{\mathcal{M}_{jk}}\}_{(j,k) \in \{1, \dots, R\}^2}$, $A_{\mathcal{M}_{jk}} = \underline{m}_j \cdot \underline{m}_k$, $\underline{\pi}(\underline{z}) = [\pi_i(\underline{z})]_{i=1, \dots, R}$, $\underline{b} = [b_i]_{i=1, \dots, R}$, $b_i = \underline{z} \cdot \underline{m}_i$.

Cramer's rule can be then applied to retrieve the elements in $\underline{\pi}(\underline{z})$ [16], [17]. Specifically, let us consider $\underline{A}_{\mathcal{M}} = [A_{\mathcal{M}_1} | \dots | A_{\mathcal{M}_j} | \dots | A_{\mathcal{M}_R}]$, where $A_{\mathcal{M}_j}$ identifies the j th column of $\underline{A}_{\mathcal{M}}$. Thus, let us define $\underline{A}_{\mathcal{M}}^{(h)}$ as the matrix obtained by replacing the h th column of $\underline{A}_{\mathcal{M}}$ with \underline{b}^T . Thanks to the above mentioned Cramer's rule

$$\pi_h(\underline{z}) = |\det[\underline{A}_{\mathcal{M}}^{(h)}]| \cdot |\det[\underline{A}_{\mathcal{M}}]|^{-1}. \quad (5)$$

Recalling that the general cross-correlation coefficient definition for two multidimensional signals $\underline{\theta}$ and $\underline{\zeta}$ over the same support is $\rho_{\underline{\theta}\underline{\zeta}} = (\underline{\theta} \cdot \underline{\zeta}) / (|\underline{\theta}| |\underline{\zeta}|)$, $|\det[\underline{A}_{\mathcal{M}}]|$ can be computed as a function of the cross-correlation coefficients between any pairs of endmembers [16].

Additionally, since the matrix $\underline{A}_{\mathcal{M}}$ is a Gram matrix in \mathcal{M} , i.e., $\underline{A}_{\mathcal{M}} = \mathcal{M} \mathcal{M}^T$ [16], [18], $\underline{A}_{\mathcal{M}}$ is positive

semidefinite. Moreover, its determinant represents the Gram determinant of the endmember set. Geometrically, the Gram determinant is the square of the volume of the parallelotope formed by the considered vectors. In particular, the vectors are linearly independent if and only if the Gram determinant is nonzero, i.e., if and only if the Gram matrix is nonsingular [16], [18], [19].

Hence, let $\Omega_{\mathcal{M}}$ be the volume of the subspace spanned by the endmember signatures, i.e., $\Omega_{\mathcal{M}} = (\det[\underline{A}_{\mathcal{M}}])^{1/2}$. According to the properties of Gramian matrices, this value is constrained

$$0 \leq \Omega_{\mathcal{M}} \leq \sqrt{\prod_{r=1}^R A_{\mathcal{M},rr}} \quad (6)$$

where $\Omega_{\mathcal{M}} \rightarrow (\prod_{r=1}^R A_{\mathcal{M},rr})^{1/2}$ when the endmembers are orthogonal. On the other hand, $\Omega_{\mathcal{M}} \downarrow 0$ when at least two spectral signatures in \mathcal{M} are linearly dependent. Thus, the first result achieved by looking at the value of $\Omega_{\mathcal{M}}$ is an estimate of the efficiency of the considered endmember set to thoroughly characterize the nonlinear interactions occurring over the scene.

Moreover, it is possible to use $\Omega_{\mathcal{M}}$ in order to obtain accurate information on the relationship among \mathcal{M} and the generic l th nonlinear residual. Indeed, let S_l be $\mathcal{M} \cup \hat{\underline{y}}_l^{(NL)}$ and let \underline{A}_{S_l} be the Gramian matrix induced by the endmembers' spectra and the l th nonlinear residual. Hence, \underline{A}_{S_l} can be written as [20], [21]

$$\underline{A}_{S_l} = \{A_{S_{ij}}\}_{(i,j) \in \{0, \dots, R\}^2} = \begin{bmatrix} \xi_{00l} & \xi_{0l} \\ \xi_{0l}^T & \underline{A}_{\mathcal{M}} \end{bmatrix} \quad (7)$$

where $\xi_{0l} = [\xi_{0il}]_{i=1, \dots, R}$, $\xi_{0il} = \hat{\underline{y}}_l^{(NL)} \cdot \underline{m}_i$ and $\xi_{00l} = \hat{\underline{y}}_l^{(NL)} \cdot \hat{\underline{y}}_l^{(NL)}$. Then, let Ω_{S_l} be the volume of the subspace spanned by the endmembers' signatures, i.e., $\Omega_{S_l} = (\det[\underline{A}_{S_l}])^{1/2}$. According to (6), $0 \leq \Omega_{S_l} \leq (\xi_{00l} \prod_{r=1}^R A_{\mathcal{M},rr})^{1/2}$. Hence, when $\hat{\underline{y}}_l^{(NL)}$ is linearly dependent on one or more spectrums in \mathcal{M} , the volume of the subspace induced by S_l tends to zero. If $\Omega_{S_l} \rightarrow (\xi_{00l} \prod_{r=1}^R A_{\mathcal{M},rr})^{1/2}$, then the l th nonlinear residual is orthogonal to all the endmembers. This means that it would be impossible to achieve accurate nonlinear UMX performance by using these endmembers over the l th pixel. Therefore, as long as $\Omega_{S_l} \downarrow 0 \forall l = 1, \dots, P$, the extracted endmembers are actually providing a solid description of the linear combinations occurring over the considered scene.

In an alternative formulation, since $\Omega_{S_l}^2 = \xi_{00l} \Omega_{\mathcal{M}}^2 + \sum_{r=1}^R (-1)^r \xi_{0rl} \det[\underline{A}_{\mathcal{M}}^{(r)}]$, one can write

$$\Omega_{S_l}^2 = \xi_{00l} \Omega_{\mathcal{M}}^2 \bar{\psi}_l \quad (8)$$

where $\bar{\psi}_l = 1 + \sum_{r=1}^R (-1)^r (\xi_{0rl} / \xi_{00l}) \pi_r (\hat{\underline{y}}_l^{(NL)})$, with $0 \leq (\bar{\psi}_l)^{1/2} \leq 1$. Hence, $\sqrt{\bar{\psi}_l}$ can be used to estimate the overall efficiency of the scheme for detecting linear mixtures.

Finally, this result can be used to compute the efficiency of the system based on \mathcal{M} as follows:

$$\eta_{\mathcal{M}} = 1 - E[\bar{\phi}] \quad (9)$$

where $\bar{\phi} = [(\bar{\psi}_l)^{1/2}]_{l=1, \dots, P}$ and $E[\bar{\phi}]$ represents the expected value of its distribution. It is worth noting that $\eta_{\mathcal{M}} \downarrow 0$ if $E[\bar{\phi}] \rightarrow 1$. In that case, \mathcal{M} would be orthogonal to every nonlinear residual. Therefore, the extracted endmembers would fail in detecting and recognizing a substantial contribution to the element combination within the scene, resulting in poor UMX performance and a jeopardized understanding of the physical phenomena.

Once the $\underline{\pi}(\underline{z})$ coefficients are computed, the terms in (3) are mapped onto a coherent space. Thus, it is possible to compute the volume induced by the polytopes identified by $\hat{\underline{D}}_l$, $\underline{y}'_l = \sum_{r=1}^R \pi_r (\hat{\underline{y}}_l^{(NL)}) \underline{m}_r$ and $\underline{D}_l^{(n)} = \sum_{r=1}^R \pi_r (\hat{\underline{d}}_l^{(n)}) \underline{m}_r$ according to the Cayley–Menger formula [18], [22].

Eventually, it is possible to provide a likelihood for linear mixture occurrence over the l th pixel as follows:

$$L_l = 1 - \frac{|V(\hat{\underline{D}}_l) - V(\underline{D}_l^{(n)})|}{|V(\hat{\underline{D}}_l) - V(\underline{y}'_l)| + |V(\hat{\underline{D}}_l) - V(\underline{D}_l^{(n)})|} \quad (10)$$

where $V(\underline{z})$ identifies the aforementioned volume of the polytope induced by \underline{z} . Further, $\hat{\underline{D}}_l$, \underline{y}'_l and $\underline{D}_l^{(n)}$ result from properly expanding and compressing the polytope induced by the endmembers in \mathcal{M} [16]. Thus, it is possible to prove that $V(\hat{\underline{D}}_l)$, $V(\underline{y}'_l)$ and $V(\underline{D}_l^{(n)})$ can be written as functions of the volume of the subspace induced by the endmember set. Specifically, $V(\hat{\underline{D}}_l) = V(\hat{\underline{d}}_l) \cdot \Omega_{\mathcal{M}}$, $V(\underline{y}'_l) = V(\underline{\pi}(\hat{\underline{y}}_l^{(NL)})) \cdot \Omega_{\mathcal{M}}$ and $V(\underline{D}_l^{(n)}) = V(\underline{\pi}(\hat{\underline{d}}_l^{(n)})) \cdot \Omega_{\mathcal{M}}$ [16]–[18].

Accordingly, (10) can be rewritten as follows:

$$L_l = 1 - \frac{|V(\hat{\underline{d}}_l) - V(\underline{\pi}(\hat{\underline{d}}_l^{(n)}))|}{|V(\hat{\underline{d}}_l) - V(\underline{\pi}(\hat{\underline{y}}_l^{(NL)}))| + |V(\hat{\underline{d}}_l) - V(\underline{\pi}(\hat{\underline{d}}_l^{(n)}))|} \quad (11)$$

The likelihood in (11) aims at providing a measure of the linearity of the mixture that occurs over each pixel in the considered hyperspectral image. Further, the process to compute L_l takes a small amount of operations and UMX inversions. Therefore, the proposed framework actually delivers a very efficient estimation of the type of spectral mixture that occurs onto the l th pixel. The following section reports the performance in detecting pixels resulting from linear mixtures on synthetic and real hyperspectral scenes.

III. EXPERIMENTAL RESULTS

To validate the proposed approach, tests on synthetic and real hyperspectral data were performed and compared, whenever possible, with the existing literature results. All the experiments and the corresponding results are reported below.

A. Synthetic Data Sets

The architecture introduced in Section II has been first tested over data sets that have been synthetically generated. We considered a data set of $P = 100 \times 100$ spectral signatures and $N = 100$ bands. Ten endmembers, randomly chosen from the USGS spectral library [23], have been used to generate each pixel in the data set. The endmembers are characterized by an average cross-correlation factor ρ , defined

TABLE I
QUANTITATIVE ANALYSIS OF THE DETECTION OF LINEAR MIXTURES OVER SYNTHETIC DATA SETS BY MEANS OF THE PROPOSED FRAMEWORK: ACCURACY (ACC = TP + TN), MISMATCH (MIS = FP + FN), AND EXECUTION TIME

p^+	SNR [dB]	ρ	ν	$\eta_{\mathcal{M}}$	TP [%]	TN [%]	FP [%]	FN [%]	ACC [%]	MIS [%]	Exec. time [msec/pixel]
2	30	0.35	1.09	0.76	48	48.1	1.9	2	96.1	3.9	18
3			1.03	0.69	47.2	48.4	2.5	1.9	95.6	4.4	18.3
4			1.05	0.563	46.9	47	2.9	3.2	93.9	6.1	18.2
5			0.98	0.52	46	47.5	3.9	3	93.1	6.9	18.2
6			0.92	0.576	45.4	49.1	4.3	1.2	94.5	5.5	18.4
			1.21	0.43	46	33.3	4.4	16.3	79.3	20.7	19.3
3	25	0.35	1.14	0.51	44.5	42.2	5.1	8.2	86.7	13.3	18.7
	30		1.03	0.69	47.2	48.4	2.5	1.9	95.6	4.4	18.3
	35		0.99	0.78	48.1	48.5	1.7	1.6	96.7	3.3	18.2
			0.25	1.031	0.84	48.8	49.1	1.2	0.9	96.3	3.7
3	30	0.35	1.03	0.69	47.2	48.4	2.5	1.9	95.6	4.4	18.3
		0.45	1.028	0.54	44.2	43.1	4.5	7.8	87.3	12.3	18.4
		0.55	1.029	0.37	44.45	34.25	5.5	15.2	78.7	21.3	18.2

TABLE II
QUANTITATIVE ANALYSIS OF THE DETECTION OF LINEAR MIXTURES OVER SYNTHETIC DATA SETS BY MEANS OF THE ALGORITHM IN [14]: ACCURACY (ACC = TP + TN), MISMATCH (MIS = FP + FN), EXECUTION TIME IN TERMS OF NVE, AND UMX

p^+	SNR [dB]	ρ	ν	$\eta_{\mathcal{M}}$	TP [%]	TN [%]	FP [%]	FN [%]	ACC [%]	MIS [%]	Exec. time [msec/pixel]		
											Total	NVE	UMX
2	30	0.35	1.09	0.76	47	46.8	2.9	3.3	93.8	6.2	40.2	31.1	9.1
3			1.03	0.69	45.5	47.9	3.7	2.9	93.4	6.6	40.1	31	9.1
4			1.05	0.563	44.8	47.6	5.7	1.9	92.4	7.6	40.4	31.2	9.2
5			0.98	0.52	45.8	45.7	4.3	4.2	91.5	8.5	40.3	31	9.3
6			0.92	0.576	47.7	42.9	5.1	4.3	90.6	9.4	40.1	30.7	9.4
			1.21	0.43	47.4	32.3	8.7	11.6	79.7	20.3	42.3	32.7	9.6
3	25	0.35	1.14	0.51	43.3	43.5	6.1	7.1	86.8	13.2	41.4	31.9	9.5
	30		1.03	0.69	45.5	47.9	3.7	2.9	93.4	6.6	40.1	30.7	9.4
	35		0.99	0.78	48.9	46.7	2.3	2.1	95.6	4.4	39.3	29.9	9.4
			0.25	1.031	0.84	45.1	48	3.8	3.1	93.1	6.9	39.6	30.1
3	30	0.35	1.03	0.69	45.5	47.9	3.7	2.9	93.4	6.6	40.1	30.3	9.8
		0.45	1.028	0.54	43.7	45.2	4.3	6.8	88.9	11.1	40.2	30.6	9.6
		0.55	1.029	0.37	44.65	36.45	6.5	12.4	81.1	18.9	39.8	30.1	9.7

as $\rho = \left(\binom{R}{2}\right)^{-1} \sum_{(i,j) \in \{1, \dots, |\mathcal{M}|\}^2, i > j} \rho_{ij}$. Specifically, each spectrum mixture has been drawn randomly from a p -linear mixing model representation: the order of the mix can be $p = 1$ or $p \in (1, p^+)$ with the same probability. Hence, the l th pixel spectrum can be written as $\underline{y}_l = \sum_{k=1}^p \sum_{r=1}^R \omega_{kr} \underline{m}_r^k$, where $\underline{m}_r^k = [m_{rn}^k]_{n=1, \dots, N}$ and $\sum_{k=1}^p \sum_{r=1}^R \omega_{kr} = 1$, $\omega_{kr} \geq 0 \forall (r, k)$. Moreover, each mixture is affected by additive white Gaussian noise with a known signal-to-noise ratio (SNR). The proportion between the energy of the nonlinear contributions and the noise variance is reported in Tables I and II as ν . Finally, the efficiency of the considered set of endmembers with respect to the given data set has been estimated according to (9) ($\eta_{\mathcal{M}}$ in Tables I and II).

The results are summarized in Table I. Specifically, estimates for (11) have been thresholded assuming a uniform distribution to discriminate mixtures into linear and nonlinear. If $L_l > 0.5$, then the l th pixel is assumed to result from a linear mixture of endmembers. Outcomes are reported in terms of true positives, true negatives, false positives, and false positives counts (TP, TN, FP, FN, respectively). Table I also reports the execution time performance in terms of msec/pixel. Apparently, the proposed architecture is very resilient to perturbations in spectral elements and noise signals. Moreover, the method is able to effectively detect the occurrence of linear mixtures also when higher order nonlinear effects are present

in the data set. The proposed method provides detection of linear mixtures with no clear dependence on the proportion of the energy of nonlinear endmember combinations, and the noise variance. Nonorthogonal projection is especially robust to ν dynamics, since accuracy performance in Table I are not apparently correlated with the ratio between nonlinear contributions and noise variance.

This effect is further highlighted in Fig. 1, which reports the accuracy of the proposed approach in detecting linear mixtures over synthetic data sets as a function of SNR when $p^+ = \{2, 3, 5\}$ (in blue, orange, and gray, respectively). Fig. 1 shows that the accuracy performances of the algorithm in Section II tend to monotonically decrease with decreasing SNR for different settings of the nonlinearities in the data sets. This result does not surprise since a low SNR implies scarce signal quality, i.e., major issues in processing records and extracting information.

As expected, the results show that, in general, when p^+ increases, the performance typically tends to degrade. However, when $p^+ = 6$ the provided detection seems to deliver slightly better estimates than the system set to $p^+ = \{4, 5\}$. This effect arises from the way the data sets are generated. In fact, the distribution of nonlinear combinations is uniform over the interval of the nonlinearity orders $(1, p^+]$. Therefore, as the p^+ increases, the number of coefficients that

TABLE III

QUANTITATIVE ANALYSIS OF THE DETECTION OF LINEAR MIXTURES OVER SYNTHETIC DATA SETS BY MEANS OF THE ALGORITHM IN [14] WHEN $P_{FA}=10^{-2}$: ACCURACY (ACC = TP + TN), MISMATCH (MIS = FP + FN), EXECUTION TIME IN TERMS OF NVE AND UMX

p^+	SNR [dB]	ρ	ν	η_M	TP [%]	TN [%]	FP [%]	FN [%]	ACC [%]	MIS [%]	Exec. time [msec/pixel]		
											Total	NVE	UMX
2	30	0.35	1.09	0.76	47.6	46.9	2.3	3.2	94.5	5.5	40.8	31.4	9.4
3			1.03	0.69	47.3	47.1	3.3	2.3	94.4	5.6	40.8	31.6	9.2
4			1.05	0.563	45.5	48	4.9	1.6	93.5	6.5	41	31.5	9.5
5			0.98	0.52	46.7	46.1	3.9	3.3	92.8	7.2	41.1	31.7	9.4
6			0.92	0.576	48.4	43.5	4.7	3.4	91.9	8.1	40.9	31.4	9.5
3	20	0.35	1.21	0.43	45.3	35.5	9.5	9.9	80.3	19.7	43	33.2	9.8
	25		1.14	0.51	44.7	43.2	6.3	5.8	87.9	12.1	42.2	32.6	9.6
	30		1.03	0.69	47.3	46.3	3.7	2.7	93.6	6.4	41.2	31.3	9.9
	35		0.99	0.78	47.4	48.5	2.1	2	95.9	4.1	40.1	30.4	9.7
3	30	0.25	1.031	0.84	45.4	48.4	3.3	2.9	93.8	6.2	40.4	30.3	10.1
		0.35	1.03	0.69	45.9	48.1	2.3	3.7	94	6	41.4	30.9	10.5
		0.45	1.028	0.54	44.2	45.2	4.1	6.5	89.4	10.6	41.1	31.3	9.8
		0.55	1.029	0.37	44.9	36.9	6.3	11.9	81.8	18.2	41.7	31.8	9.9

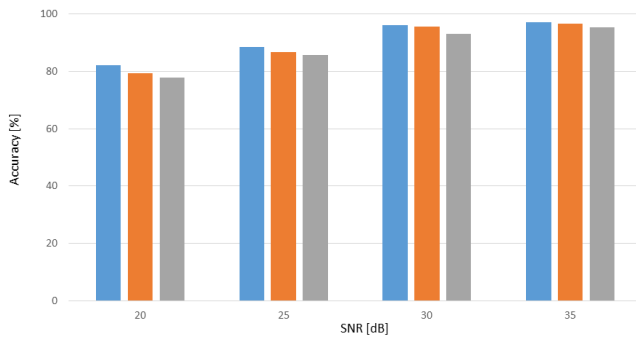


Fig. 1. Accuracy of the proposed method in detecting linear mixtures over synthetic data sets as a function of SNR when $p^+ = \{2, 3, 5\}$ (in blue, orange, and gray, respectively).

drive the nonlinear mix increases, while their counts tend to decrease. Thus, the volume of $\underline{\pi}(\hat{y}'^{(NL)})$ gets lower as well, while the distance $|V_{\hat{\delta}} - V_{\underline{\pi}(\hat{y}'^{(NL)})}|$ tends to increase, leading to a slight performance degradation. Moreover, it is possible to appreciate how the efficiency coefficient trend behaves accordingly to the aforesaid distribution of the detection accuracy.

It is important to note that the performance of the algorithm is affected by the choice of the endmember set, as mentioned in Section II. Indeed, the proposed method can provide better and more reliable knowledge of the actual kind of the mixtures over the scene when the set of endmembers is chosen such that their spectra are orthogonal to each other. This feature provides a stronger ability to detect nonlinear effects while avoiding the saturation effect provided by linearly dependent endmembers. Thus, the EEA is actually affecting the computation of the likelihood in (11). Hence, endmembers must be carefully selected such that the nonlinear effects can be properly understood and quantified within the space induced by these endmembers.

In order to assess the performance of the algorithm, we used the architecture in [14] to detect linear mixtures applied to the same synthetic images. As previously mentioned, the algorithm in [14] relies on the computation of image statistics. Specifically, it requires to compute the error $\hat{\underline{e}}$ obtained from

a least-square optimization able to invert a bilinear mixing problem.

It also estimates the noise variance $\hat{\sigma}^2$, determined as the average of the $P - R + 1$ smallest eigenvalues of the sample covariance matrix. Then, each pixel is considered to result from a linear mixture if $T^* = \hat{\underline{e}}^T \hat{\underline{e}} / \hat{\sigma}^2 < \eta$, where η is a function of the chosen probability of false alarm P_{FA} , i.e., $\eta = \vartheta(1 - P_{FA})$, being ϑ the inverse cumulative distribution function of the χ^2 distribution with $P - R + 1$ degrees of freedom. In order to provide a fair comparison with the results achieved by means of our proposed framework, we applied [14] and set the P_{FA} according to the probability of false alarm obtained by our approach. We also conducted experiments using $P_{FA} = 10^{-2}$ in order to guarantee that the method in [14] is not unnecessarily considering nonlinear pixels within the analysis.

Tables II and III report the results achieved by using this *a posteriori* test. It is possible to appreciate that the method proposed in this paper outperforms the algorithm in [14] in terms of accuracy over almost all the proposed test cases. Moreover, the proposed architecture strongly reduces latency. This effect is due to the fact that in [14] the whole image variance has to be computed. In fact, the noise variance estimation (NVE) causes most of the overhead introduced by the method in [14]. Therefore, the efficiency of the proposed approach relies on the two inversions in (1) and (2), which apparently require a smaller amount of time with respect to the statistical investigation in [14].

Furthermore, it is worth noting that the detection performance of the architecture in [14] does not show apparent correlations to the η_M parameter, such that it can slightly outperform the proposed approach when $\eta_M \lesssim 0.5$. This result is motivated by use of a single UMX scheme, which decouples the accuracy from the endmember space. Indeed, investigating the type of mixture of each pixel without considering the properties of the subspace implicitly requires to rely on the image statistics, which provides a source of additional aggregate information of the scene mixture distribution. In turn, this effect leads to inaccurate description of the intrinsic mixture feature delivered by every pixel, as well as to a significant latency overhead. Even setting the P_{FA} according

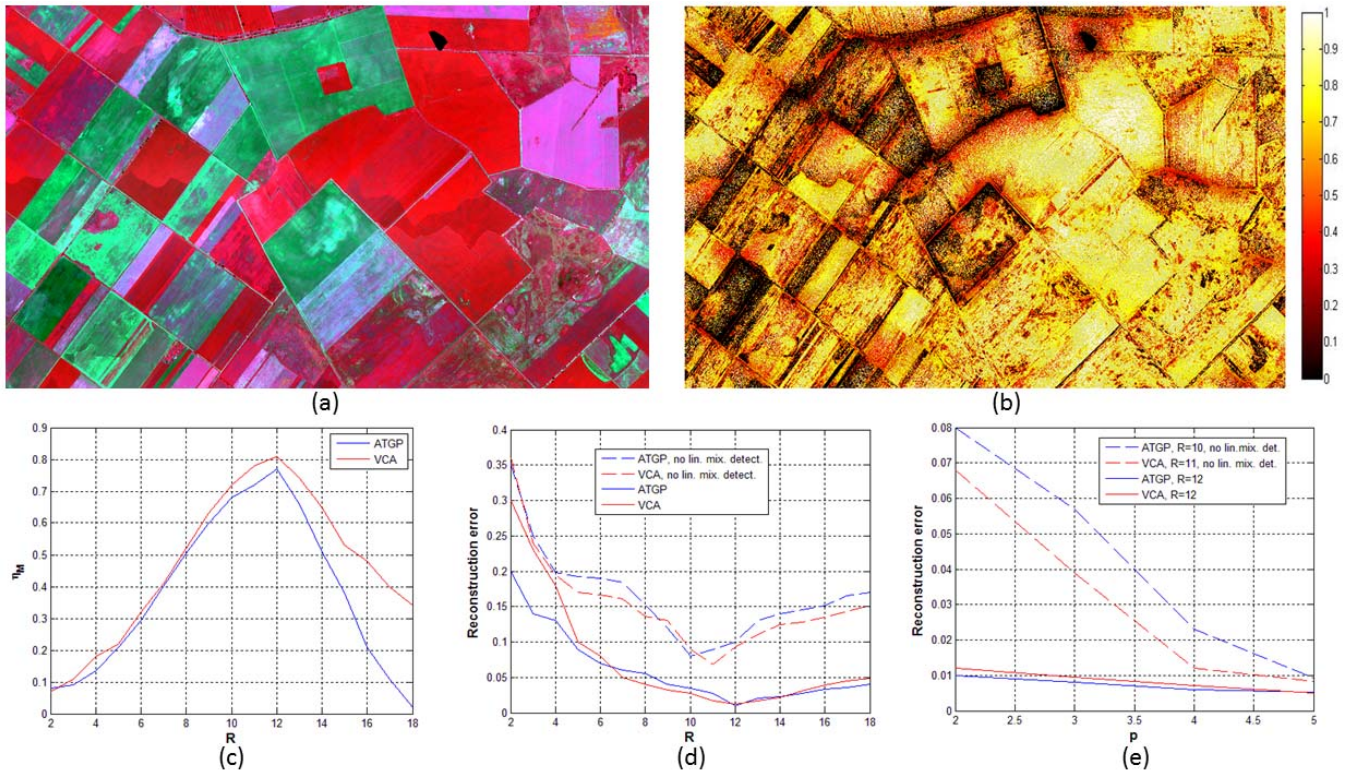


Fig. 2. Linear detection result of the Heves test site. (a) False color composite of the arable lands nearby the town of Heves, Hungary. (b) Distribution of the L_1 coefficients as in (11) when the ATGP method has been used to extract 12 endmembers. (c)–(e) Efficiency and RE performance as a function of the used EEA, the number of considered endmembers, the nonlinearity order, and the UMX framework that is employed.

to [14] does not change the detection performance of this method (Table III).

B. Real Data Sets

To further illustrate the suitability of the new model, we tested the proposed method on two real hyperspectral images. The first data set identifies an image recorded by AISA Eagle sensor, which contains 614×507 pixels mosaicked using two flightlines over the arable lands in the area nearby the town of Heves, Hungary [Fig. 2(a)]. 252 bands ranging from 395 to 975 nm in the visible and NIR spectral range have been acquired. The area is not only useful because of agricultural production, but nearby is an important bird habitat frequently monitored by the BirdLife Hungary NGO. Thus, although the original ground spatial resolution of the image was 2 m, the image was downsampled to 6-m ground resolution while keeping the original spectral information as possible, such that the data set could be used for the purposes of land cover interpretation.

Fig. 2(b) shows the distribution of the L_1 coefficients estimated according to (11) for this image. It is possible to note how the most of the linear mixtures detected according to the proposed approach occur over checkerboard fields, which are most likely to realize linear mixing of the scattered energy.

Moreover, Fig. 2(c) shows the distribution of the efficiency index computed along (9) when the automatic target generation process (ATGP) [24] and vertex component analysis (VCA) [25] methods have been used to extract endmembers (in blue and red lines, respectively). It is possible

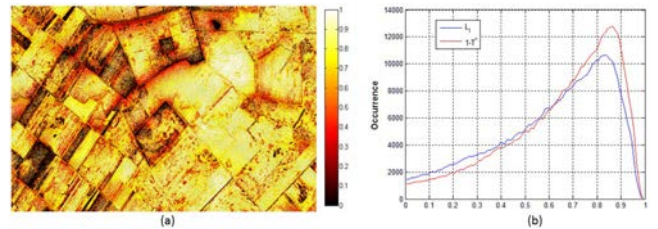


Fig. 3. (a) Distribution of the $1 - T^*$ test as in [14] when the ATGP method has been used to extract 12 endmembers over the Heves image. (b) Occurrence histogram of the L_1 (blue line) and $1 - T^*$ (red line).

to appreciate that η_M reaches its maximum when the number of endmembers R is set to 12. In other words, the convex hull provided by the considered 12 endmembers represents the best solution to describe the nonlinear contributions delivered by all the spectral signatures involved in the given data set. Finally, it is possible to note that the efficiency delivered by VCA is always larger than the one provided by ATGP. This result is caused by the implicit properties of the considered EEAs. Indeed, VCA computes the best signatures that can be used to build up a simplex that contains the considered data cloud. On the other hand, ATGP identifies the best pool of spectra to describe the spectral mixtures within the data set itself. Therefore, ATGP is by definition more prone than VCA to deliver endmembers that are less orthogonal to each other. However, it is important to note that ATGP is also more robust than VCA to deliver endmember spectra that are close to the physical reality of the scene.

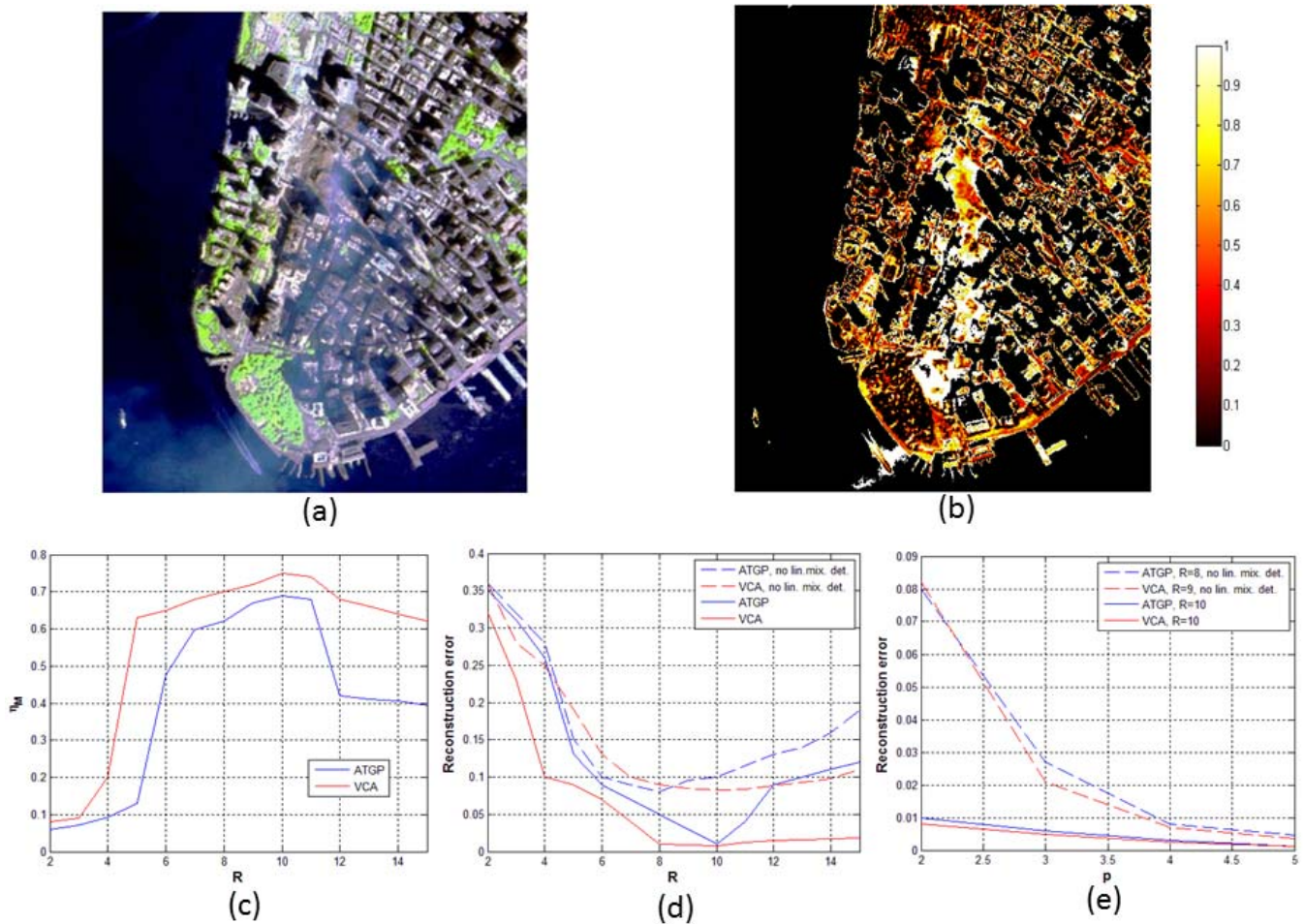


Fig. 4. Linear detection result for the NYC test site. (a) False color composite of the WTC area. (b) Distribution of the L_1 coefficients as in (11) when the ATGP method has been used to extract ten endmembers. (c)–(e) Efficiency and RE performance as a function of the used EEA, the number of considered endmembers, the nonlinearity order, and the UMX framework that is employed.

Fig. 2(d) and (e) shows the reconstruction error (RE) performance of the UMX framework that has been proposed, where $RE = ((1/PN) \sum_{l=1}^P \|y_l - \hat{y}_l\|^2)^{1/2}$ and \hat{y}_l identifies the reconstructed spectral signature of the l th pixel obtained by means of FCLS. Specifically, Fig. 2(d) displays the RE distribution as a function of the number of endmembers R that have been extracted by means of ATGP (blue lines) and VCA (red lines). The nonlinearity order used for reconstruction of the spectral mixtures is set to 2. The minimum RE performance is achieved when $R = 12$ endmembers are used, i.e., when the efficiency is maximum. Thus, the proposed approach is apparently able to identify the best pool of endmembers that can be used to characterize the spectral combinations that occur over the given data set. Moreover, the proposed architecture is actually able to enhance the UMX performance with respect to classic nonlinear UMX schemes, as shown by the RE curves obtained when the detection of linear mixtures has not been employed yet [dashed lines in Fig. 2(d)]. Further, the minimum RE performance achieved when the proposed detection of linear mixtures is not employed occurs for $R < 12$. This effect results because the UMX scheme is strongly affected by overfitting, since the

bilinear scheme tries to characterize the spectral signatures in the data set according to the bilinear model for each pixel and the reconstructed spectra are affected by fluctuations induced by the model mismatch with respect to the physical reality of the hyperspectral scene.

Fig. 2(e) shows the RE behavior as a function of the nonlinearity order p used to design the mixture model. The curves identify the processing chains that have been previously described when reporting the results in Fig. 2(d). Moreover, the number of endmembers R that have been considered has been set to 12 when the linear mixture detection that has been proposed in this paper has been employed. On the other hand, if the linear mixtures are not detected, $R = 10$ and 11 endmembers are considered when ATGP and VCA are used to extract endmembers. This setting has been considered in order to provide a fair comparison between the minimum RE performance delivered by the considered UMX schemes. It is possible to appreciate how the proposed architecture enhanced by linear mixture detection dramatically outperforms classic nonlinear UMX. This effect is highlighted when low nonlinearity orders are considered.

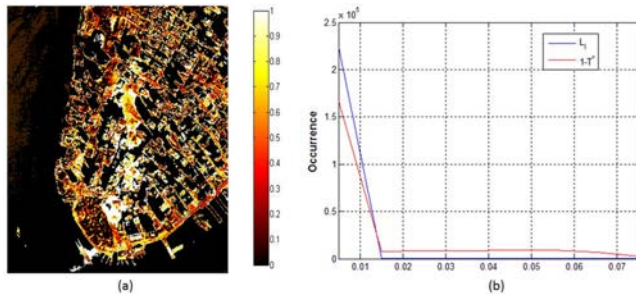


Fig. 5. (a) Distribution of the $1 - T^*$ test as in [14] when the ATGP method has been used to extract ten endmembers over the NYC image. (b) Occurrence histogram of the L_I (blue line) and $1 - T^*$ (red line).

Even in this case, it is interesting to compare the achieved results to those obtained by means of the method in [14]. In fact, the performance of the proposed approach can be further assessed when the results in Fig. 2(b) are compared with the distribution of the T^* test computed as in [14]. Fig. 3(b) reports the histograms of $1 - T^*$ (which is proportional to the likelihood of detecting linear mixtures according to the algorithm in [14]) and L_I over the Heves image, while Fig. 3(a) graphically provides the distribution of T^* test results [to be compared with Fig. 2(b) for L_I]. Apparently, the $1 - T^*$ test is less selective than L_I , as it assigns high scores to pixels closer to the field borders, which are indeed likely to be produced by nonlinear mixtures of elements.

A second test for the proposed procedure is the World Trade Center (WTC) image collected by AVIRIS on 16 September 2001 in New York City (NYC). The full data set consists of 614×507 pixels, with $N = 224$ bands and a spatial resolution of 1.7 m/pixel. Fig. 4(a) shows a false color composite of an image acquired over the WTC area. Moreover, Fig. 4(b) shows the distribution of the likelihoods of detected linear mixtures over the WTC area. Note that the proposed approach correctly does not detect any linear mixtures over water areas, because water is characterized by strong nonlinear combinations [26]. Fig. 4(c)–(e) displays the same quantities as Fig. 2(c)–(e). The maximum efficiency is obtained for $R = 10$. This effect arises from the fact that the WTC image is much more heterogeneous than the rural scene in Fig. 2(a). Thus, EEAs are less prone to detect highly correlated endmembers, resulting in higher overall orthogonality of the endmember set, i.e., a larger volume of the subspace induced by endmember signatures. The trends in Fig. 2(d) and (e) are confirmed by the curves in Fig. 4(d) and (e).

Further, as in the previous data set, we compared the distributions of $1 - T^*$ and L_I . These distributions are in agreement over most of the image. Differences are notable in water areas, where it is worth to highlight that the method in [14] assigns higher scores than the L_I metrics. Fig. 5(b) further emphasizes this aspect, since it shows the occurrence of the estimated L_I and $1 - T^*$ lower values.

IV. CONCLUSION

A novel method for the detection of linear mixtures in hyperspectral data sets has been introduced. The proposed algorithm takes advantage of the geometrical features that a

least squares optimization of the mixed spectra provides, such that *a priori* estimates can be delivered. The experimental results show that this approach is able to deliver accurate performances in detecting linear mixtures over artificial and natural considered scenes by means of a framework with low computational cost.

Specifically, the outcomes of this paper are as follows:

- 1) a new approach for detecting linear mixtures in hyperspectral images has been introduced;
- 2) an accurate estimate of the type of mixtures by means of nonorthogonal mapping onto the subspace induced by the endmembers;
- 3) low computational costs required to run the proposed framework as algorithms based on fast optimization are employed;
- 4) as no *a posteriori* tests are required, the proposed method efficiently implements a low complexity algorithm for an *a priori* detection of the nature of the spectral mixtures.

We are currently working toward extending the framework developed in this paper to provide a qualitative detection of linear mixtures and an enhanced EEA.

REFERENCES

- [1] R. Heylen, M. Parente, and P. Gader, "A review of nonlinear hyperspectral unmixing methods," *IEEE J. Sel. Topics Appl. Earth Observ. Remote Sens.*, vol. 7, no. 6, pp. 1844–1868, Jun. 2014.
- [2] N. Dobigeon, J.-Y. Tourneret, C. Richard, J. C. M. Bermudez, S. McLaughlin, and A. O. Hero, "Nonlinear unmixing of hyperspectral images: Models and algorithms," *IEEE Signal Process. Mag.*, vol. 31, no. 1, pp. 82–94, Jan. 2014.
- [3] J. M. Bioucas-Dias *et al.*, "Hyperspectral unmixing overview: Geometrical, statistical, and sparse regression-based approaches," *IEEE J. Sel. Topics Appl. Earth Observ. Remote Sens.*, vol. 5, no. 2, pp. 354–379, Apr. 2012.
- [4] A. Marinoni and P. Gamba, "A novel approach for efficient p -linear hyperspectral unmixing," *IEEE J. Sel. Topics Signal Process.*, vol. 9, no. 6, pp. 1156–1168, Sep. 2015.
- [5] A. Marinoni, A. Plaza, and P. Gamba, "Harmonic mixture modeling for efficient nonlinear hyperspectral unmixing," *IEEE J. Sel. Topics Appl. Earth Observ. Remote Sens.*, vol. 9, no. 9, pp. 4247–4256, Sep. 2016.
- [6] R. Heylen and P. Gader, "Nonlinear spectral unmixing with a linear mixture of intimate mixtures model," *IEEE Geosci. Remote Sens. Lett.*, vol. 11, no. 7, pp. 1195–1199, Jul. 2014.
- [7] R. Close, P. Gader, J. Wilson, and A. Zare, "Using physics-based macroscopic and microscopic mixture models for hyperspectral pixel unmixing," *Proc. SPIE*, vol. 8390, p. 83901L, May 2012.
- [8] J. Broadwater, R. Chellappa, A. Banerjee, and P. Burlina, "Kernel fully constrained least squares abundance estimates," in *Proc. IEEE Int. Geosci. Remote Sens. Symp. (IGARSS)*, Barcelona, Spain, Jul. 2007, pp. 4041–4044.
- [9] A. Marinoni, J. Plaza, A. Plaza, and P. Gamba, "Nonlinear hyperspectral unmixing using nonlinearity order estimation and polytope decomposition," *IEEE J. Sel. Topics Appl. Earth Observ. Remote Sens.*, vol. 8, no. 6, pp. 2644–2654, Jun. 2015.
- [10] Y. Altmann, N. Dobigeon, and J.-Y. Tourneret, "Nonlinearity detection in hyperspectral images using a polynomial post-nonlinear mixing model," *IEEE Trans. Image Process.*, vol. 22, no. 4, pp. 1267–1274, Apr. 2013.
- [11] Y. Altmann, N. Dobigeon, S. McLaughlin, and J.-Y. Tourneret, "Residual component analysis of hyperspectral images—Application to joint nonlinear unmixing and nonlinearity detection," *IEEE Trans. Image Process.*, vol. 23, no. 5, pp. 2148–2158, May 2014.
- [12] Y. Altmann, N. Dobigeon, S. McLaughlin, and J.-Y. Tourneret, "Unsupervised post-nonlinear unmixing of hyperspectral images—Application to a Hamiltonian Monte Carlo algorithm," *IEEE Trans. Image Process.*, vol. 23, no. 6, pp. 2663–2675, Jun. 2014.
- [13] H.-C. Li and C.-I. Chang, "Linear spectral unmixing using least squares error, orthogonal projection and simplex volume for hyperspectral images," in *Proc. IEEE WHISPERS*, Tokyo, Japan, Jun. 2015, pp. 2–5.

- [14] Y. Altmann, N. Dobigeon, J.-Y. Tourneret, and J. C. M. Bermudez, "A robust test for nonlinear mixture detection in hyperspectral images," in *Proc. IEEE ICASSP*, Vancouver, BC, Canada, May 2013, pp. 2149–2153.
- [15] D. C. Heinz and C.-I. Chang, "Fully constrained least squares linear spectral mixture analysis method for material quantification in hyperspectral imagery," *IEEE Trans. Geosci. Remote Sens.*, vol. 39, no. 3, pp. 529–545, Mar. 2001.
- [16] G. E. Bredon, *Topology Geometry*. New York, NY, USA: Springer-Verlag, 1993.
- [17] L. N. Trefethen and D. Bau, III, *Numerical Linear Algebra*. Philadelphia, PA, USA: SIAM, 1997.
- [18] I. N. Herstein, *Topics in Algebra*, 2nd ed. Hoboken, NJ, USA: Wiley, 1975.
- [19] V. Kaibel and A. Schwartz, "On the complexity of polytope isomorphism problems," *Graphs Combinat.*, vol. 19, no. 2, pp. 215–230, 2003.
- [20] G. H. Golub and C. F. Van Loan, *Matrix Computations*, 3rd ed. Baltimore, MD, USA: The Johns Hopkins Univ. Press, 1996.
- [21] V. V. Prasolov, *Problems and Theorems in Linear Algebra*. Providence, RI, USA: AMS, 1991.
- [22] R. Heylen, D. Burazerovic, and P. Scheunders, "Non-linear spectral unmixing by geodesic simplex volume maximization," *IEEE J. Sel. Topics Signal Process.*, vol. 5, no. 3, pp. 534–542, Jun. 2011.
- [23] R. N. Clark, G. A. Swayze, A. J. Gallagher, T. V. V. King, and W. M. Calvin, "The U.S. Geological Survey, digital spectral library: Version 1 (0.2 to 3.0 μm)," USGS Open File Rep., vol. 93, no. 592, 1993.
- [24] H. Ren and C.-I. Chang, "Automatic spectral target recognition in hyperspectral imagery," *IEEE Trans. Aerosp. Electron. Syst.*, vol. 39, no. 4, pp. 1232–1249, Oct. 2003.
- [25] J. M. Bioucas-Dias and J. M. P. Nascimento, "Hyperspectral subspace identification," *IEEE Trans. Geosci. Remote Sens.*, vol. 46, no. 8, pp. 2435–2445, Aug. 2008.
- [26] Y. Altmann, A. Halimi, N. Dobigeon, and J.-Y. Tourneret, "Supervised nonlinear spectral unmixing using a postnonlinear mixing model for hyperspectral imagery," *IEEE Trans. Image Process.*, vol. 21, no. 6, pp. 3017–3025, Jun. 2012.



Andrea Marinoni (S'07–M'11–SM'16) received the B.Sc., M.Sc. (*cum laude*), and Ph.D. degrees in electronic engineering from the University of Pavia, Pavia, Italy, in 2005, 2007, and 2011, respectively.

In 2009, he was a Visiting Researcher at the University of California, Los Angeles, Los Angeles, CA, USA. Since 2011, he has been a Post-Doctoral Fellow at the Telecommunications and Remote Sensing Laboratory, Department of Electrical, Computer, and Biomedical Engineering, University of Pavia.

Since 2015, he has been a short-term Visiting Researcher at the Earth and Planetary Image Facility, Ben-Gurion University of the Negev, Be'er Sheva, Israel. Since 2016, he has been a Visiting Researcher at the School of Geography and Planning, Sun Yat-Sen University, Guangzhou, China, and a short-term Visiting Researcher at the School of Computer Science, Fudan University, Shanghai, China. His research interests include efficient nonlinear signal processing applied to hyperspectral unmixing, astroinformatics and big data mining, analysis, and management for human–environment interaction assessment.

Dr. Marinoni was a recipient of the two-year "Dote Ricerca Applicata" Award in 2011, sponsored by the Region of Lombardy, Italy, and STMicroelectronics N.V. He was an Invited Speaker at the 2010 Workshop on Application of Communication Theory to Emerging Memory Technologies, the IEEE Global Communications Conference (GLOBECOM), Miami, FL, the 2014 New Challenges in Astro- and Environmental Informatics in the Big Data Era Workshop, Szombathely, Hungary, the Big Data Methodologies in Remote Sensing and Astronomy Special Session at the 2015 IEEE Geoscience and Remote Sensing Symposium, Milan, Italy, and the 2015 Astroinformatics, Dubrovnik, Croatia.



Antonio Plaza (M'05–SM'07–F'15) received the M.Sc. and Ph.D. degrees in computer engineering from the University of Extremadura, Badajoz, Spain, in 1999 and 2002, respectively.

He is currently the Head with the Hyperspectral Computing Laboratory, Department of Technology of Computers and Communications, University of Extremadura. He has authored more than 500 publications, including 193 JCR journal papers (over 140 in IEEE journals), 23 book chapters, and 285 peer-reviewed conference proceeding papers. His research interests include hyperspectral data processing and parallel computing of remote sensing data.

Dr. Plaza is a Fellow of the IEEE "for contributions to hyperspectral data processing and parallel computing of Earth observation data." He was a recipient of the recognition of Best Reviewers of the IEEE GEOSCIENCE AND REMOTE SENSING LETTERS in 2009 and the Best Reviewers of the IEEE TRANSACTIONS ON GEOSCIENCE AND REMOTE SENSING in 2010, for which he served as an Associate Editor from 2007 to 2012. He was also a recipient of the Best Column Award of the IEEE SIGNAL PROCESSING MAGAZINE in 2015, the 2013 Best Paper Award of the IEEE JOURNAL OF SELECTED TOPICS IN APPLIED EARTH OBSERVATIONS AND REMOTE SENSING (JSTARS), the most highly cited paper (2005–2010) in the *Journal of Parallel and Distributed Computing*, and the Best Paper Awards at the IEEE International Conference on Space Technology and the IEEE Symposium on Signal Processing and Information Technology. He is also an Associate Editor of the IEEE ACCESS. He was a member of the Editorial Board of the IEEE GEOSCIENCE AND REMOTE SENSING NEWSLETTER from 2011 to 2012 and the IEEE GEOSCIENCE AND REMOTE SENSING MAGAZINE in 2013. He was also a member of the steering committee of JSTARS. He served as the Director of Education Activities for the IEEE Geoscience and Remote Sensing Society (GRSS) from 2011 to 2012, and is currently serving as the President of the Spanish Chapter of IEEE GRSS. He has reviewed over 500 manuscripts for over 50 different journals. He is currently serving as the Editor-in-Chief of the IEEE TRANSACTIONS ON GEOSCIENCE AND REMOTE SENSING. He has guest edited 10 special issues on hyperspectral remote sensing for different journals.



Paolo Gamba (SM'00–F'13) received the Laurea (*cum laude*) degree in electronic engineering and the Ph.D. degree in electronic engineering from the University of Pavia, Pavia, Italy, in 1989 and 1993, respectively.

He is currently a Professor of telecommunications with the University of Pavia, where he leads the Telecommunications and Remote Sensing Laboratory and serves as the Deputy Coordinator with the Ph.D. School in Electronics and Computer Science. He has authored more than 130 papers in international peer-review journals and presented more than 250 research works in workshops and conferences.

Dr. Gamba served as the Editor-in-Chief of the IEEE GEOSCIENCE AND REMOTE SENSING LETTERS from 2009 to 2013, and as the Chair of the Data Fusion Committee of the IEEE Geoscience and Remote Sensing Society (GRSS) from 2005 to 2009. Currently, he serves as the GRSS Vice President for Professional Activities, the Chair of the Chapters Committee, and the Chair of the Symposium Awards Committee. He has been the Organizer and Technical Chair of the Biennial GRSS/ISPRS Joint Workshops on "Remote Sensing and Data Fusion over Urban Areas" since 2001. He also served as the Technical Co-Chair of the 2010 and 2015 IGARSS conferences, Honolulu, HI, USA, and Milan, Italy, respectively. He has been the Guest Editor of Special Issues of the IEEE TRANSACTIONS ON GEOSCIENCE AND REMOTE SENSING, the IEEE JOURNAL OF SELECTED TOPICS IN REMOTE SENSING APPLICATIONS, the *ISPRS Journal of Photogrammetry and Remote Sensing*, and the *International Journal of Information Fusion and Pattern Recognition Letters* on the topics of urban remote sensing, remote sensing for disaster management, and pattern recognition in remote sensing applications. He has been invited to give keynote lectures and tutorials in several occasions about urban remote sensing, data fusion, EO data, and risk management.